Hybrid conducting alginate-based hydrogel for lactate biosensing

Ismael Babeli,[a] Anna Puiggalí-Jou,[a,b,*] Joan Josep Roa,[b,c] Maria-Pau Ginebra,[b,d,e] Jose García-Torres[b,d,*] and Carlos Alemán[a,b,e,*]

[a] *Departament d'Enginyeria Química, EEBE, Universitat Politècnica de Catalunya, C/ Eduard Maristany, 10-14, 08019, Barcelona, Spain*

[b] *Barcelona Research Center in Multiscale Science and Engineering, Universitat Politècnica de Catalunya, 08930 Barcelona, Spain*

[c] *Center for Research in Structural Integrity, Reliability and Micromechanics of Materials, Departament de Ciència i Enginyeria de Materials, Universitat Politècnica de Catalunya, 08030 Barcelona, Spain*

[d] *Biomaterials, Biomechanics and Tissue Engineering Group, Departament de Ciència i Enginyeria de Materials, Universitat Politècnica de Catalunya (UPC), 08930 Barcelona, Spain*

[e] *Institute for Bioengineering of Catalonia (IBEC), Barcelona Institute of Science and Technology (BIST), Baldiri Reixac 10-12, 08028 Barcelona Spain*

[*] anna.puiggali@upc.edu,

jose.manuel.garcia-torres@upc.edu and carlos.aleman@upc.edu

Abstract

A biosensor based on a conducting nanocomposite hydrogel is developed for the detection of L-lactate. The hydrogel is based on a mixture of alginate (Alg) and poly(3,4-ethylenedioxythiophene) (PEDOT), which is loaded with gold nanoparticles (GNP). Alg provides 3D structural support and flexibility, PEDOT confers conductivity and sensing capacity, and GNP provides signal amplification with respect to simple voltammetric and chronoamperometric response. In the optimized conditions, the nanocomposite hydrogel is able to detect hydrogen peroxide with linear response and limits of detection of 0.91 μM and 0.02 μM by cyclic voltammetry and chronoamperometry, respectively. The optimized hydrogel is functionalized by the glutaraldehyde method with lactate oxidase enzyme, which catalyzes the oxidation of L-lactate to pyruvate in the presence of dissolved oxygen, forming hydrogen peroxide. For L-lactate detection, the functionalized biosensor works in two linear regimes, one for concentrations lower than 5 mM with a limit of detection of 0.4 mM, and the other for concentrations up to 100 mM with a limit of detection of 3.5 mM. The developed biosensor could be suitable for a wide number of biological fluids in which the L-lactate concentration ranges from 1.6 to 20.4 mM (before exercise) and from 7.2 to 62.2 mM (after exercise).

Introduction

Alginate hydrogels (Alg-h) have attracted great attention as biomaterial in applications like extracellular matrices [1,2] vehicles for drug delivery [3-6], refillable drug depots for targeted delivery [7] and scaffolds for tissue engineering [8-10]. Alginate (Alg) is a linear polysaccharide composed of homopolymeric blocks of 1,4-linked of D-mannuronic acid (M) and L-glucoronic acid (G) [11]. The M block segments are linear and flexible while the G blocks are rigid, providing stiffness as a result of the steric hindrance around the carboxylic groups, which is due the 1,4-linkage. Although they can be prepared using small poly(carboxylic acid) compounds and dimethyl sulfoxide [12], Alg-h are commonly obtained by ionic crosslinking through combination of Alg with divalent cations, which interact with G monomers blocks to form tightly held ionic bridges (*i.e.* divalent ions interact with four-carboxyl groups forming the well-known egg-box arrangement [13]). On the contrary, blocks of M monomers form weak junctions with divalent cations.

In recent years, conductive Alg-h (cAlg-h) have been prepared combining alginic acid with carbon nanofibers [14], carbon nanotubes [15] and conducting polymers [16-20] (CPs). These materials have been used for manufacturing tissue engineering scaffolds [14,16,20], sensors to detect microbial activity [15], energy storage devices [17] and mechanical sensors [18,19]. The utilization of CPs is particularly striking for the preparation of cAlg-h, which have been attributed not only to their wide technological use (*e.g.* energy storage devices [21], anticorrosive coatings [22] and electrochromic devices [23]) but also to recent advances in their biomedical applications [24-26]]. Within the latter context, the utilization of CPs as electrochemical sensors to detect biomolecules is particularly relevant because of their redox properties [24-28].

Among CPs, poly(3,4-ethylenedioxythiophene) (PEDOT) is an ideal candidate for the development of bioelectronic devices because of its high electrical conductivity, environmental and chemical stability (even in biological media), fast doping-dedoping capacity, good electrochemical properties and biocompatibility [29-31]. Furthermore, CPs can be tuned with metallic nanoparticles (NP) to form composites with better electrical and electrochemical properties. Among the metallic NP, noble metals in general and gold in particular has been the most used due to its exceptional electric conductivity, stability and biocompatibility [32-33]. On the other hand, the combination of PEDOT with polysaccharides, such as Alg, could result not only in an improvement of the biocompatibility and electrochemical stability in physiological media but also in a more flexible composite as the polysaccharide confers 3D structural support and flexibility to the electroactive materials.

In this study, an electrochemically active hydrogel composed of Alg and PEDOT, and loaded with gold nanoparticles (GNP), has been prepared for use as L-lactate biosensor. In the resulting composite hydrogel, hereafter denoted Alg/PEDOT/GNP-h, the polysaccharide acts as a flexible support, while the CP provides electrochemical activity. The role of the loaded spherical GNP is to enhance the conductivity, the electron transport and the electrocatalytic capacity of the system for reducing hydrogen peroxide (H_2O_2) to OH^-. The functionalization of Alg/PEDOT/GNP-h with lactate oxidase (LOx) results in a flexible, biocompatible and efficient L-lactate sensor by detecting the H_2O_2 produced by the enzymatic oxidation of L-lactate to pyruvate.

Methods

Materials

Sodium alginate (Mw= 240 kDa), poly(3,4-ethylenedioxythiophene) : polystyrene sulfonate (PEDOT:PSS) suspension (1.3 wt.%), chloroauric acid (HAuCl$_4$), lactate oxidase (LOx) and sodium citrate (Na$_3$Ct) were obtained from Sigma-Aldrich. Calcium chloride (CaCl$_2$) was purchased from Scharlab. Milli-Q water grade (0.055 S/cm) was used in all solutions and synthetic processes.

Synthesis of GNP

GNP were prepared using the method developed by Turkevich [34], which regulates the particle size by controlling the citrate / gold ratio [35]. The product of this method, which follows a seed-mediated growth mechanism, is a monodisperse gold suspension coming from the chemical reduction of a metallic salt. Specifically, 10 mg of HAuCl$_4$ in 100 mL deionized water was heated to 100 °C under vigorous stirring. Next, 3 mL of Na$_3$Ct at 1%, which acted as both reducing and capping agent, were added into the solution for stabilizing the nanoparticles. The resulting suspension was vigorously stirred for 30 min when a color change was appreciated (*i.e.* from yellowish to red wine color, which is typical of spherical GNP). Finally, the suspension was cooled to room temperature.

Synthesis of hydrogels

In addition to the Alg/PEDOT/GNP-h, two different hydrogels were prepared as controls: *i*) Alg-h; and *ii*) a hydrogel composed of Alg and PEDOT but without GNP, hereafter named Alg/PEDOT-h. To control the dimensions of the prepared hydrogels, silicone molds with dimensions $200 \times 50 \times 2$ mm^3 were fabricated with Ecoflex® 00-10 (a platinum cure silicon rubber compound) and filled with 200 μL of the precursor solutions.

For the synthesis of the hydrogels, a 3.9 wt.% alginic acid solution was prepared by dissolving the biopolymer in deionized water at 50 ℃ with vigorous stirring for 1 h. Alg-h were obtained by immersing the molds filled with the alginic acid solution into a $CaCl_2$ 3 wt.% solution for 24 h. Then, the excess of $CaCl_2$ was removed by washing the samples with milli-Q water.

For the preparation of Alg/PEDOT-h, equal volumes of the commercial 1.3 wt% PEDOT:PSS dispersion and the 3.9% wt.% alginic acid solution were mixed at room temperature with vigorous stirring for 20 min. Hydrogels were formed by immersing the silicon rubber molds filled with the mixture into a $CaCl_2$ 3 wt.% aqueous solution for 24 h. As above, Alg/PEDOT/GNP-h were prepared using the same procedure but adding a concentration of 2 nM, 6 nM or 30 nM to the mixture.

For some characterizations, hydrogels were formed by depositing the corresponding precursor solution onto the ITO (indium thin oxide) side of an ITO-coated polyethylene terephthalate (PET) film.

Characterization

Transmission electron microscopy (TEM) images were obtained with a Philips TECNAI 10 electron microscope operating at 100 kV. Bright field micrographs were taken with an SIS MegaView II digital camera. Dispersions containing GNP were deposited on glow discharged carbon coated copper grids (300 mesh).

Dynamic light scattering (DLS) studies were performed using NanoBrook Omni Zeta Potential Analyzer from Brookheaven Instruments. Measurement consisted of 3 runs of 120 s duration each, which were averaged to obtain the effective diameter.

UV-vis studies were conducted on a Shimadzu 3600 spectrophotometer using quartz cuvettes. Spectra were recorded from 300 to 800 nm wavelength range.

Scanning electron microscopy (SEM) studies were performed to examine the morphology of hydrogels. Samples, which were previously cleaned and lyophilized, were placed in a focused ion beam Zeiss Neon 40 scanning electron microscope operating at 5 kV, equipped with an energy dispersive X-ray (EDX) spectroscopy system. GNP-loaded hydrogels were examined using both the secondary and backscattered electron detectors.

Attenuated total reflectance Fourier transform infrared spectroscopy (ATR-FTIR) spectra were obtained with a FTIR 4100 spectrophotometer equipped with a diamond crystal (Specac model MKII Golden Gate Heated Single Reflection Diamond ATR). The samples were evaluated using spectra manager software. For each sample, 64 scans were performed between 4000 and $600cm^{-1}$ with a resolution of $4cm^{-1}$ at room temperature.

Structural fingerprints were also characterized by micro-Raman spectroscopy using a commercial Renishaw inVia Qontor confocal Raman microscope. The Raman setup consisted of a laser (at 785 nm with a nominal 500 mW output power) directed through a microscope (specially adapted Leica DM2700 M microscope) to the sample, after which the scattered light is collected and directed to a spectrometer with a 1200 lines·mm^{-1} grating. The exposure time was 10 s, the laser power was adjusted to 1% of its nominal output power and each spectrum was collected with 3 accumulations.

Transmission electron microscopy (TEM) studies were performed using a JEOL J1010 (filament: tungsten) equipped with a Gatan *Orius* 1000 slow scan *CCD* and the DigitalMicrograph (Gatan) software. The accelerating voltage was 80 kV. A Sorvall Porter-Blum microtome (Sorwall, NT, USA) equipped with a diamond knife was used to cut the sample in thin sections that were subsequently lifted onto carbon-coated grids.

Mechanical properties, hardness (H) and elastic modulus (E), at the submicrometric length scale were determined by nanoindentation by means of a Nanoindenter XP (MTS) unit, equipped with a continuous stiffness measurement mode (CSM), allowing a dynamic determination of the mechanical properties during the indentation process [36]. Indentations were arranged in a homogeneous spaced array of 36 imprints (6 × 6). The distance between imprints was kept constant at 50 μm, in order to avoid any overlapping effect. They were done under displacement control mode at 1000 nm of maximum displacement onto the surface. Results were averaged in order to have statistical significance. Strain rate was held constant at 0.05 s^{-1} and the indenter shape was carefully calibrated for true indentation depth as small as 25 nm by indenting fused silica standard of known Young's modulus of 72 GPa [36]. The values of H and E were directly determined by means of the Oliver and Pharr method [36,37].

All electrochemical experiments were run in triplicate using the Autolab PGSTAT302N equipment. Experiments were performed in a three-electrode cell containing 10 mL of 0.1 M $CaCl_2$ solution as supporting electrolyte at room temperature. Saturated Ag|AgCl, a platinum sheet and the different hydrogels served as reference, counter and working electrodes, respectively. Cyclic voltammograms were recorded in the potential range from –0.80 to 0.80 V at a scan rate of 100 mV/s. Chronoamperometry was performed at –0.80 V. All electrochemical experiments were performed in triplicate.

Results and discussion

Preparation and characterization of hydrogel composites

The spherical morphology of GNP, which were 14.5 ± 1.8 nm in size, was observed by TEM (Figure 1a). Nanoparticles spontaneously assemble into small agglomerates, as

confirmed by DLS and UV-Vis spectroscopy (below). Colloidal suspensions prepared using different concentrations of GNP showed, by DLS, that the average size increases with the concentration (Figure 1b): 37 ± 7, 55 ± 2 and 262 ± 36 nm for 2 nM, 6 nM and 30 nM GNP, respectively. It is worth noting that DLS analyses, which do not discriminate between individual nanoparticles and agglomerates, provide good indications on the tendency to aggregate not only through average size but also through the dispersion of the average value, which grows with the concentration. As it was expected, the GNP diameter obtained by DLS for the lowest concentration was significantly larger than the one seen by TEM (*i.e.* 37 ± 7 nm *vs* 14.5 ± 1.8 nm). This was mainly attributed to the fact that the former technique measures the total hydrodynamic radius, while TEM measurements provide only with the diameter of the nanoparticles themselves.
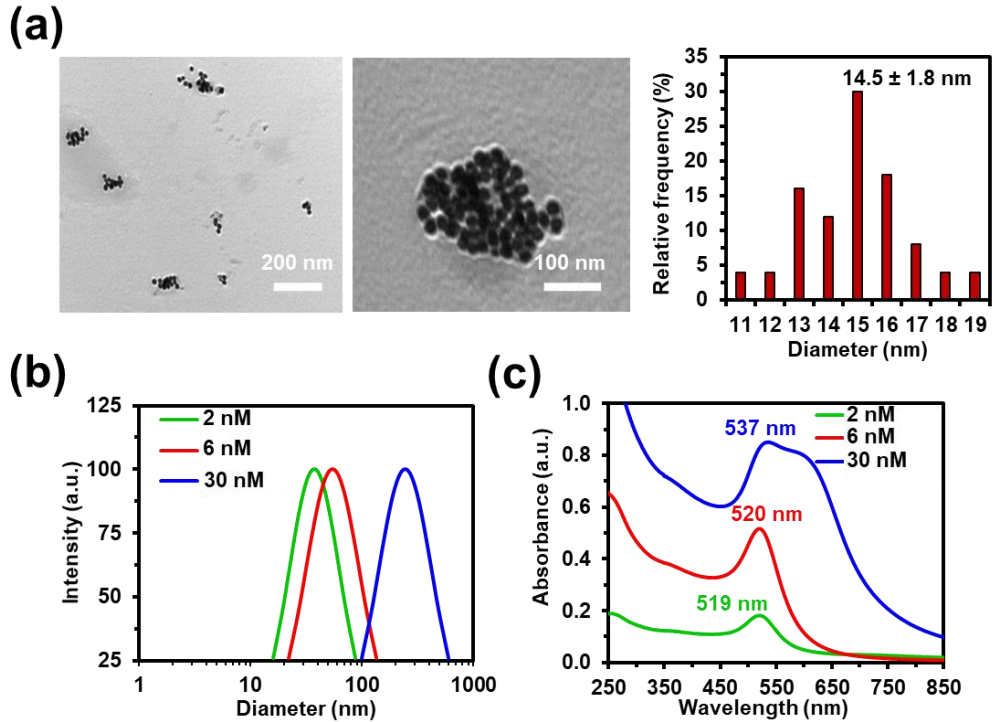

Figure 1. (a) TEM micrographs of GNP with its corresponding diameter histogram. (b) DLS (c) and UV-Vis absorption spectra of different concentrations of 2 nM, 6 nM and 30 nM GNP.

The aggregation of GNP with concentration was also monitored by UV-Vis spectroscopy (Figure 1c). The position and magnitude of the absorption band are strongly dependent on the size of the nanoparticles, the refractive index of the solvent used and the degree of aggregation [38]. The absorption shows strong resonance at 519 nm in the 2 nM dispersion due to the excitation of surface plasmon vibrations, which is a typical plasmon resonance band for individual GNPs [38]. As the concentration of nanoparticles increases, the surface plasmon resonance band shifts toward higher wavelengths due to the aforementioned aggregation. More specifically, the surface plasmon absorption band undergoes a red-shift to 520 and 537 nm for the 6 and 30 nM dispersions, respectively.

Alg-h, Alg/PEDOT-h and Alg/PEDOT/GNP-h were prepared as described in the Methods sections. In the case of Alg/PEDOT/GNP-h, GNP concentrations of 2 nM, 6 nM or 30 nM were considered, the resulting hydrogels being denoted Alg/PEDOT/GNP(xnM)-h (where x= 2, 6 or 30), respectively. Characterization studies on GNP-containing hydrogels have been mainly focused on those prepared with a GNP concentration of 6 nM since, due to its electrochemical properties, Alg/PEDOT/GNP(6nM)-h was selected for the construction of the L-lactate sensor.

Figure 2a displays photographs of the three prepared hydrogels deposited on a glass substrate. As it can be seen, Alg-h exhibited a whitish color, while Alg/PEDOT-h and Alg/PEDOT/GNP(6nM)-h showed the typical dark blue color of the CP. On the other hand, SEM micrographs of the cross-sections of hydrogels are presented in Figure 2b. Comparison of Alg-h and Alg/PEDOT-h reveals that the second presents a much more open structure with bigger pores. This effect is less pronounced when Alg-h is compared with Alg/PEDOT/GNP(6nM)-h than with Alg/PEDOT-h indicating that GNP

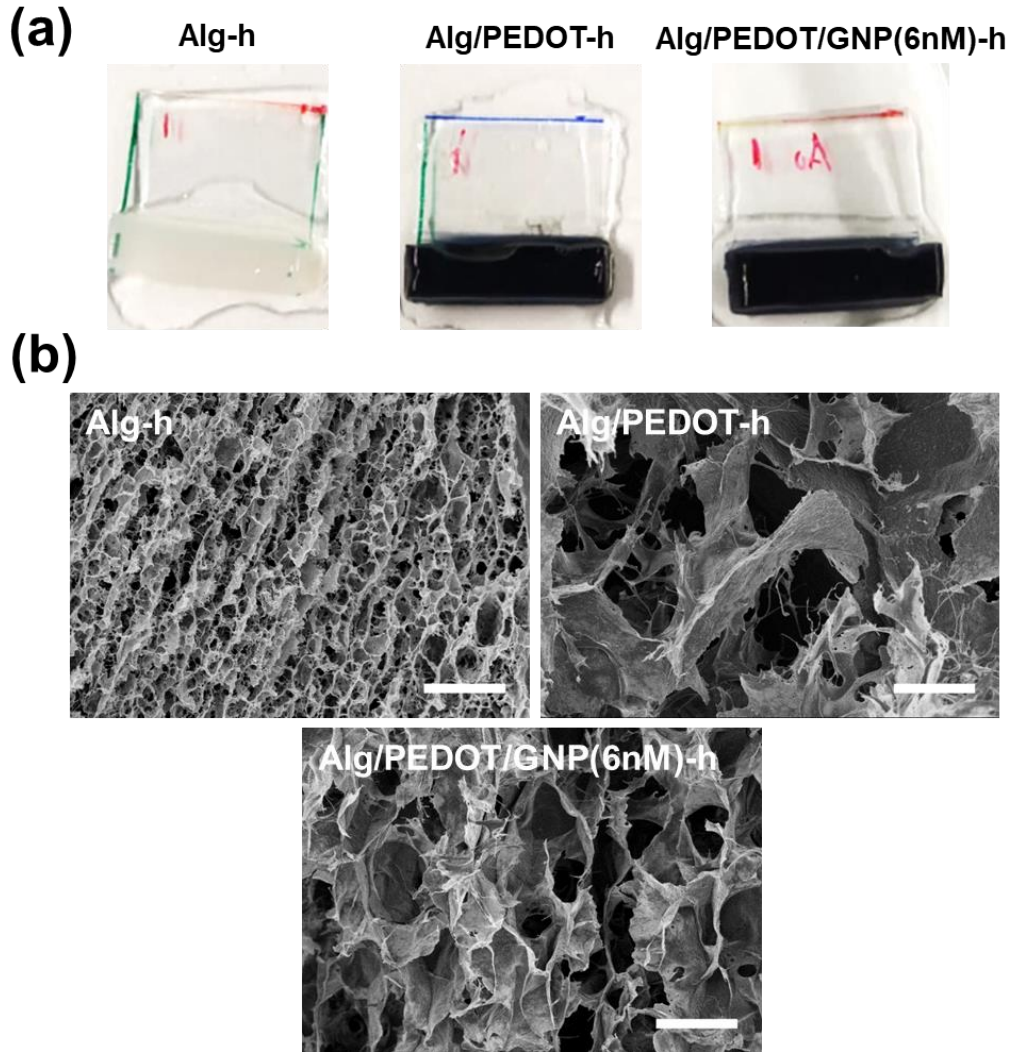have a closing effect. However, the influence of the CP on the hydrogel morphology clearly dominates over that of GNP.

Figure 2. (a) Photographs and (b) cross-sectional SEM micrographs of the prepared hydrogels: Alg-h, Alg/PEDOT-h, and Alg/PEDOT/GNP(6nM)-h. Scale bar: 100 μm.

Loaded nanoparticles in GNP-containing hydrogels were identified by backscattered electron imaging for high resolution cross-sectional SEM. This is illustrated in Figure 3, which displays a representative high-resolution micrograph in secondary electron (SE) and in backscattered electron (BSE) modes for Alg/PEDOT/GNP(6nM). High electron density elements have more substantial electron-backscattering intensities than low electron density elements and, therefore, they can be visualized as high contrast areas in

the BSE mode. Thus, GNP are clearly observed as white spots in the BSE image, confirming the success of the loading process. Nanoparticles were found to be randomly disseminated over the entire hydrogel volume, forming stable and uniform distributions, as proved the intensity profile included in Figure 3. This profile, which crosses three nanoparticles, shows that the distance associated to the intensity step is very similar in all three cases (*i.e.* from 25 to 29 nm).
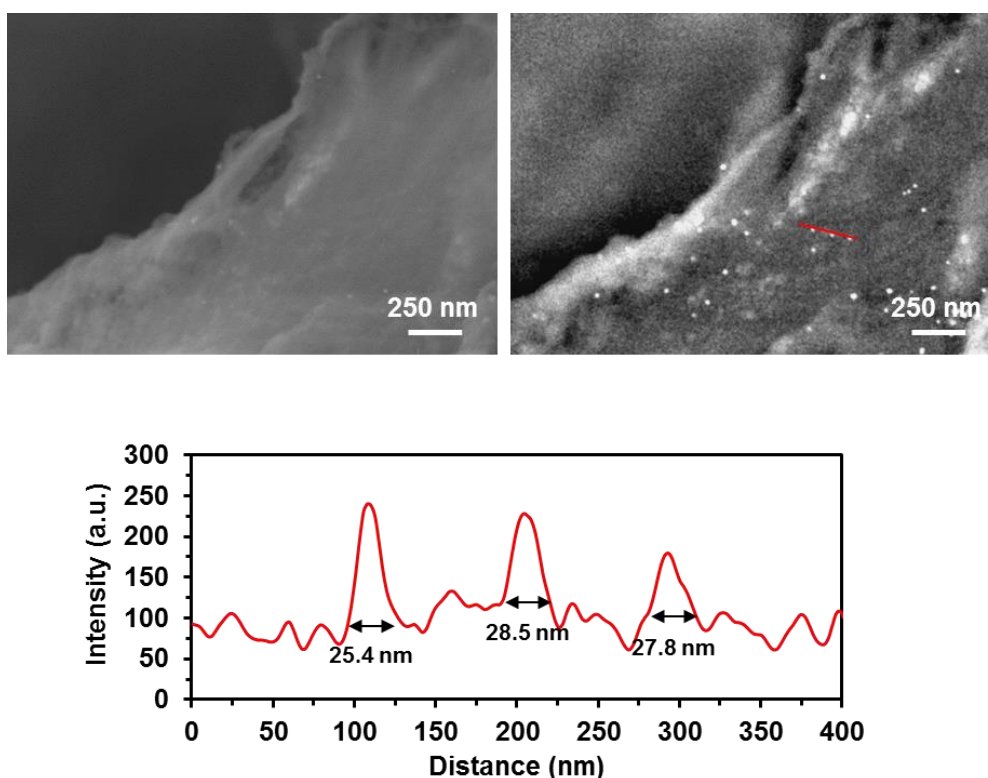

Figure 3. SEM micrographs of Alg/PEDOT/GNP(6nM) in the SE (left) and BSE (right) modes. The intensity profile displayed in the bottom row corresponds to the red line draw in the image recorded using the BSE mode.

FTIR spectra of Alg-h, Alg/PEDOT-h and Alg/PEDOT/GNP(6nM)-h are compared in Figure 4a, showing that all spectra were dominated by Alg bands. Significant peaks for Alg were detected in all samples (dashed grey lines). The O–H stretching vibrations appeared at around 3332 cm^{-1}, while C=O stretching vibration associated at the carboxylate groups was split into the asymmetric and symmetric vibration modes at

1590 and 1408 cm^{-1}, respectively. On the other hand, Alg/PEDOT-h and Alg/PEDOT/GNP(6nM)-h showed characteristic bands at 1521 and 1290 cm^{-1}, which correspond to the stretching modes of C=C and C–C in the thiophene ring, respectively. In addition, Alg/PEDOT/GNP(6nM)-h samples exhibited a weak band at 2929 cm^{-1} attributed to the C–H stretching of Na$_3$Ct. Since Na$_3$Ct is a capping agent for GNP, its presence in the spectra corroborates the incorporation of the GNP within the hydrogel [39].
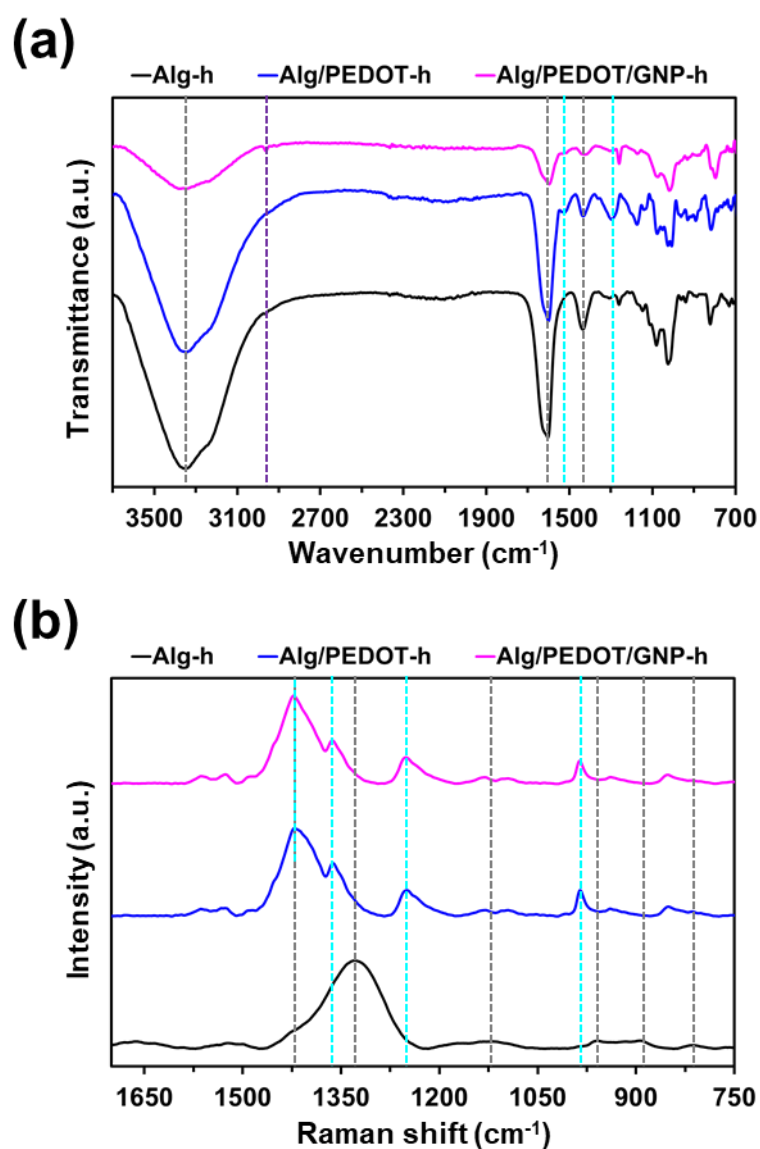
Figure 4. (a) FTIR and (b) Raman spectra of Alg-h, Alg/PEDOT-h and Alg/PEDOT/GNP(6nM)-h. Grey and blue dashed lines indicate the main peaks of Alg and PEDOT, respectively.

The Raman spectra of the three studied hydrogels are displayed in Figure 4b. The spectrum of Alg-h shows the symmetric carboxylate stretching and the C–O single bond stretching vibrations at 1427 and 1325 cm^{-1}, respectively, the skeletal vibrations at 961, 885 and 809 cm^{-1}, and the glycosidic ring breathing mode at 1121 cm^{-1} [40]. Alg peaks are hidden in Alg/PEDOT-h and Alg/PEDOT/GNP-h spectra, in which the CP bands predominate over Alg bands due to the resonance effect. Thus, the intensity of PEDOT peaks was enhanced due to the coincidence of the frequency of the electronic transition and the laser energy [41]. Alg/PEDOT-h and Alg/PEDOT/GNP-h shows the typical PEDOT fingerprints with bands at 986, 1253, 1362 and 1423 cm^{-1}, which correspond to the vibration mode of the thiophene C–S bond, C–C inter-ring stretching, C–C stretching and C=C symmetrical stretching, respectively.

In order to get better understanding on the distribution of the two polymeric phases in conducting hydrogels, TEM images of stained and unstained Alg/PEDOT-h samples were recorded (Figure 5a). Representative micrographs of stained samples show the interpenetration of high contrast (dark) zones, which are associated to the anionic sites of Alg selectively stained with a 1% uranyl acetate (UAc) solution, and bright zones (grey) that are rich in PEDOT (Figure 5a1-a3). This interpretation is corroborated by micrographs of unstained samples (Figure 5a4) in which the electron scattering properties of PEDOT predominate. Thus, the interpenetration of Alg- and PEDOT-rich zones indicates that the electrochemical properties of Alg/PEDOT-h and Alg/PEDOT/GNP-h (see below) are due to the fact that the two polymers are not segregated in completely separated phases.
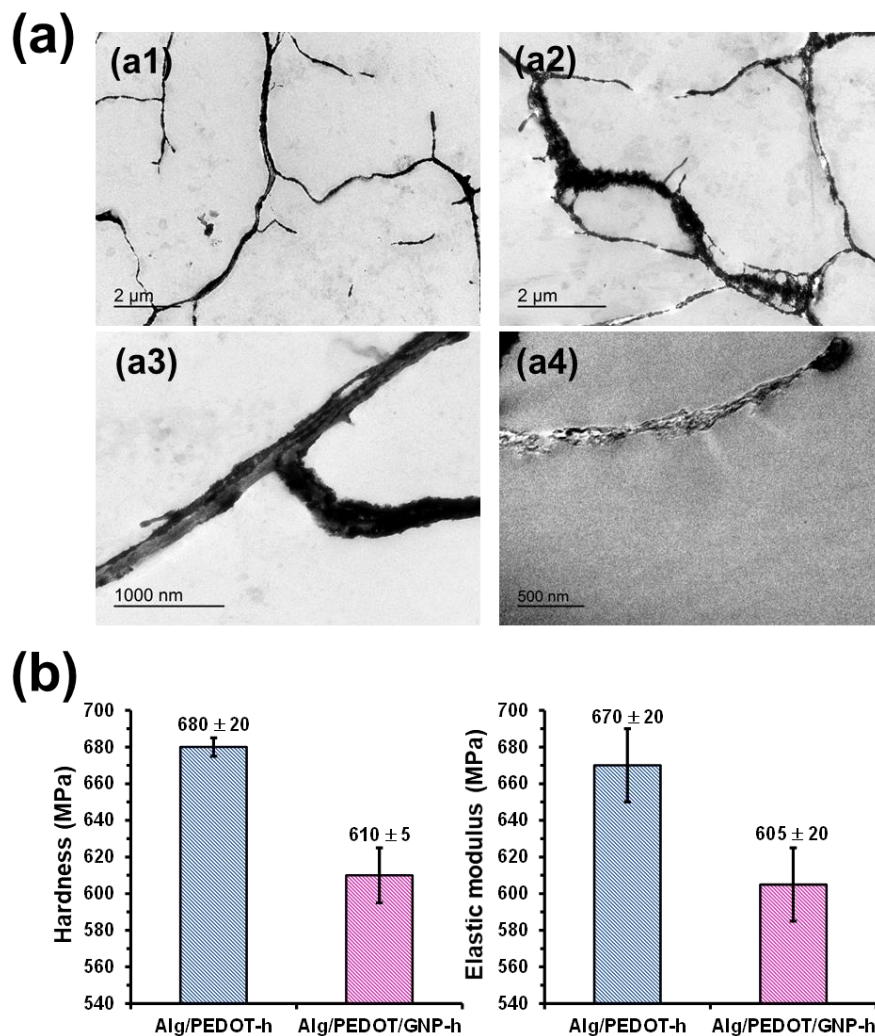
14

Figure 5. (a) TEM micrographs of Alg/PEDOT-h samples stained with UAc (a1-a3) and unstained (a4). (b) Hardness and elastic modulus of Alg/PEDOT-h and Alg/PEDOT/GNP(6nM)-h as determined by nanoindentation.

The effect of GNP on the mechanical properties of Alg/PEDOT-h was investigated at the micrometric length scale by nanoindentation. Figure 5b compares the hardness and the elastic modulus of Alg/PEDOT-h and Alg/PEDOT/GNP(6nM)-h. As it can be seen, a slight decrease in hardness and elastic modulus is observed for the GNP-containing hydrogel. The presence of the nanoparticles can diminish the number of interactions between Alg chains, which could explain the small decrease in the mechanical properties. It is worth noting that the elastic modulus of Alg/PEDOT-h is only slightly lower than that of Alg-h, even though the stiffness of the latter is known to depend on

15

the content of Ca^{2+} [42]. On the other hand, comparison of the mechanical response of the studied hydrogels with that of 5-layered films formed by 3 nanolayers of polylactic acid separated by two layers of PEDOT [43], which was also determined by nanoindentation, reveals that films exhibited lower hardness (0.18 ± 0.08 GPa) and higher elastic modulus (3.4 ± 0.2 GPa).

The electrochemical properties of Alg-h, Alg/PEDOT-h and Alg/PEDOT/GNP(x nM)-h (x= 2, 6 and 30 nM) were studied by cyclic voltammetry (CV) in a potential range from –0.80 V to 0.80 V. Alg-h show no oxidation-reduction peaks it was expected for a non-electroactive gel polymer electrolyte with ionic mobility (Figure 6a). However, an increase in the current density is observed at negative potentials due to water reduction to hydrogen. On the other hand, the incorporation of PEDOT into the hydrogel (Alg/PEDOT-h) increases the current density (j) in the whole potential range as well as the area of the voltammogram. For example, the cathodic j increases (in absolute value) up to –18 μm/cm^2 at –0.8V which is 2 times higher regarding the j for Alg-h (–9 μm/cm^2) at such potential (Figure 6b). These changes in the voltammogram can be explained by the higher electrical conductivity of the Alg/PEDOT-h compared to Alg-h and the pseudocapacitive behavior of PEDOT. Finally, while the incorporation of a low amount of GNP into the hydrogel (2 nM) does not seem having a significant effect on the CV behavior, the incorporation of a higher amount of GNP (6 nM) leads to an increase of j in the cathodic region, leading to a nearly three-fold increase in j (–50 μm/cm^2) at –0.8V compared to Alg/PEDOT-h (Figure 6b). Such increase is mainly attributed to the well-known catalytic behavior of GNP towards water reduction. A further increase in the GNP content (30 nM) does not increase the current density which is probably attributed to the aggregation of the nanoparticles, as previously seen by DLS and UV-Vis spectroscopy; thus, avoiding an effective increase of the surface area of the

16

Alg/PEDOT/GNP (30 nM)-h compared to Alg/PEDOT/GNP (6 nM)-h. According to the previous results, we selected the Alg/PEDOT/GNP(6nM)-h to further investigate its performance as L-lactate biosensor.
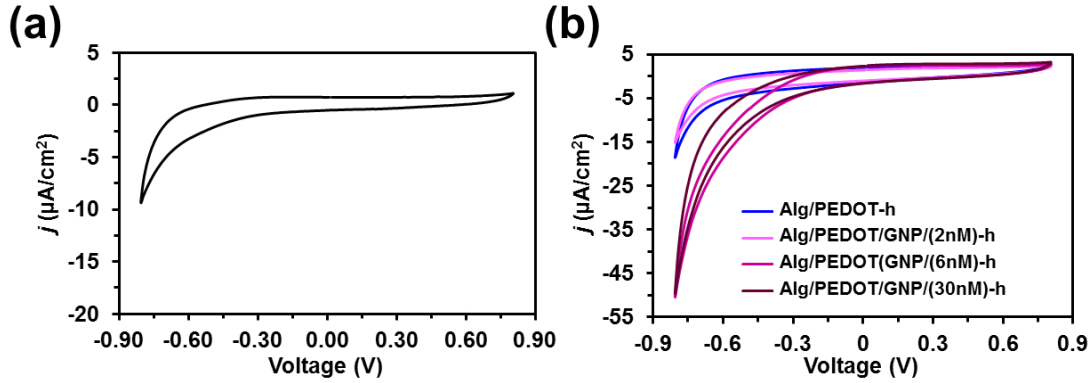

Figure 6. Cyclic voltammograms of the prepared hydrogels: (a) Alg-h; and (b) Alg/PEDOT-h, Alg/PEDOT/GNP(2nM)-h, Alg/PEDOT/GNP(6nM)-h and Alg/PEDOT/GNP(30nM)-h), using a potential range from –0.8 V to 0.8 V at a scan rate of 100 mV/s

Hydrogen peroxide detection

Electrochemical enzymatic L-lactate sensors are categorized in two groups depending on the enzyme employed: L-lactate oxidase (LOx) and L-lactate dehydrogenase (LDH) [44]. LOx catalyzes the oxidation of L-lactate to pyruvate in the presence of dissolved oxygen, forming hydrogen peroxide (H_2O_2), while LDH catalyzes the oxidation of lactate to pyruvate in the presence of the oxidized form of NAD+, forming NADH [45]. Both H_2O_2 and NADH are electrochemically active and can be reduced or oxidized, providing a current proportional to the L-lactate concentration. However, difficulties in incorporating NAD+/NADH coenzymes into the electrodes (*i.e.* coenzymes act as mediators to shuttle electrons between the enzyme and electrodes), as well as their regeneration, limits the development of LDH-based sensors, reasons why the LOx enzyme is more used in the construction of L-lactate biosensors [46]. In order

to explore the potential utilization of the developed hydrogels for manufacturing LOx-based biosensors, in this work we have focused on their electrochemical response to H_2O_2.

The response of Alg-h (control), Alg/PEDOT-h and Alg/PEDOT/GNP(6nM) to 100 mM L-lactate, 2.5 mM H_2O_2 or 100 mM H_2O_2 solutions are compared by CV in Figure 7. As it was expected, the voltammograms of all hydrogels recorded in the 100 mM L-lactate solution were practically indistinguishable from that of the blank electrolyte (*i.e.* the solution without L-lactate and H_2O_2). This was attributed to fact that LOx was not immobilized on the hydrogels surface yet. Alg-h did not show either significant changes in the CV to 5 mM or 100 mM H_2O_2 solutions. On the other hand, while Alg/PEDOT-h did not exhibit any current change to the lowest H_2O_2 concentration (2.5 mM), the current density clearly increased (in absolute value) when the concentration of H_2O_2 reached 100 mM. This response was attributed to the electrochemical reduction of $H_2O_2(aq)$ to $OH^-(aq)$:

$$H_2O_2 \ (aq) \ +2 \ e^- \rightarrow 2 \ OH^- \ (aq) \qquad\qquad (1)$$
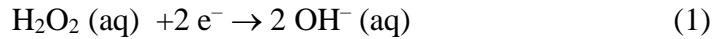
, favored by the presence of PEDOT but only at the highest concentration. Finally, Alg/PEDOT/GNP(6nM)-h showed higher current densities (in absolute value) than Alg/PEDOT-h for the two examined concentrations, which is explained by the catalytic effect of GNP to H_2O_2 reduction (Figure 7d). Thus, the current density at –0.8V increased from –18 $\mu A/cm^2$ for Alg-h to –312 $\mu A/cm^2$ for Alg/PEDOT-h or –431 $\mu A/cm^2$ for Alg/PEDO/GNP(6nM)-h in the 100 mM H_2O_2, reflecting the effect of PEDOT and GNP towards H_2O_2 reduction.
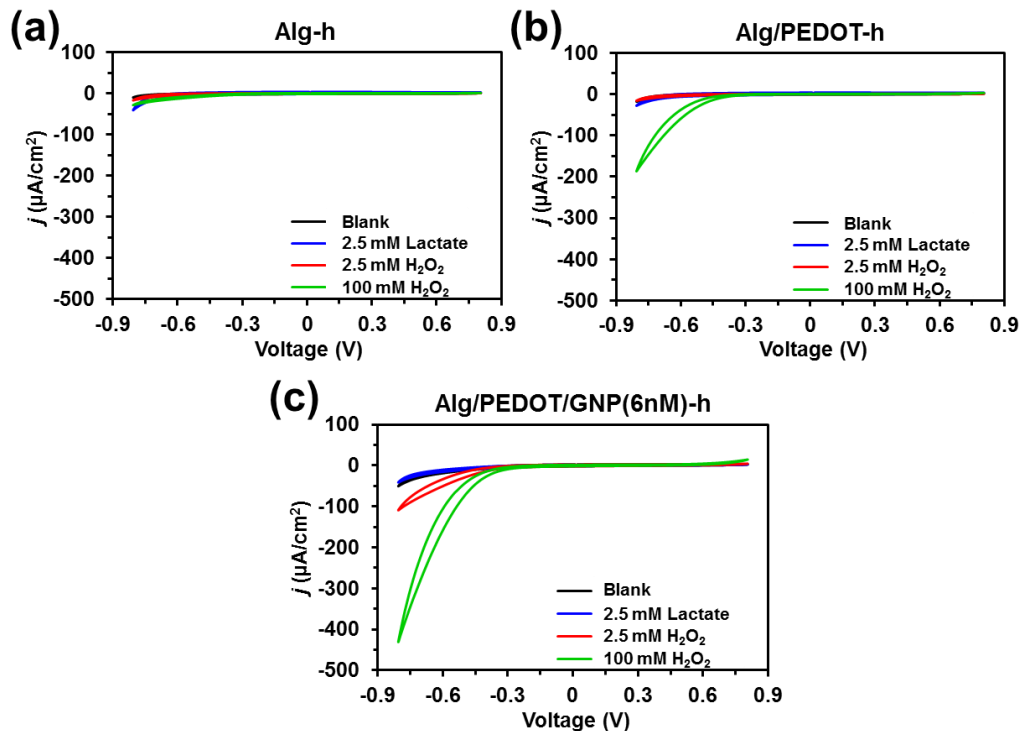
Figure 7. Cyclic voltammograms recorded from –0.8 V to 0.8 V at a scan rate of 100 mV/s for (a) Alg-h, (b) Alg/PEDOT-h and (c) Alg/PEDOT/GNP(6nM)-h. For each hydrogel, the displayed voltammograms correspond to the blank solution and the solution containing 100 mM L-Lactate, 2.5 mM H_2O_2 or 100 mM H_2O_2.

As the sensitivity of Alg/PEDOT/GNP(6nM)-h towards H_2O_2 is higher than that of Alg/PEDOT-h, smaller concentrations of H_2O_2 were considered for a more precise evaluation of the former. Figure 8a shows the cyclic voltammograms recorded for H_2O_2 solutions from 0.1 to 10 mM. The calibration plot, which was obtained using three independent repetitions for each H_2O_2 concentration, indicates that the current density (in absolute value) at –0.8V linearly increases with increasing H_2O_2 concentration (Figure 8b). Within the studied interval of concentrations, the accuracy of Alg/PEDOT/GNP(6nM)-h sensor is very high, as is reflected by the R-squared value of the calibration plot (R^2= 0.988). The sensitivity, which was derived from the absolute value of the slope of the calibration plot, is 0.128 µA/(cm^2·mM), while the limit of detection (LOD), calculated as the ratio between three times the standard deviation of

19

the blank (*i.e.* without H_2O_2) and the absolute value of the slope of the calibration curve [47], is 0.91 μM.
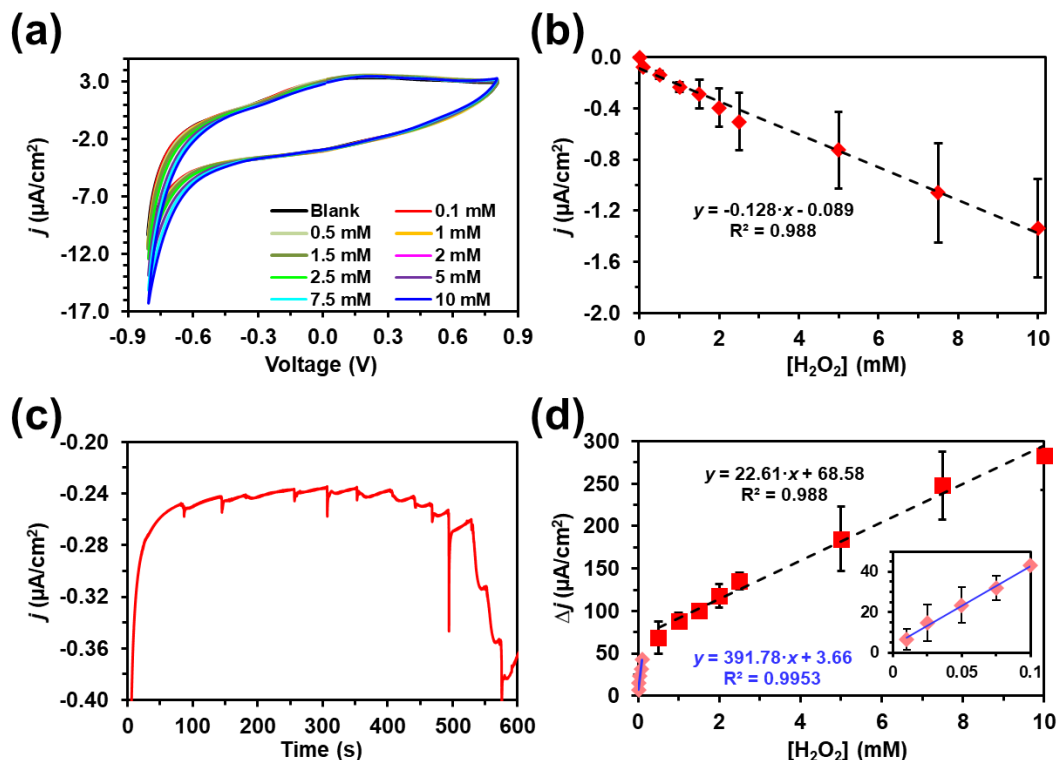

Figure 8. (a) Cyclic voltammograms recorded from –0.8 to 0.8 V at a scan rate of 100 mV/s for Alg/PEDOT/GNP(6nM)-h using solutions with different concentrations of H_2O_2, from 0 (blank) to 10 mM. (b) Calibration plot obtained from graph (a). (c) Chronoamperogram for Alg/PEDOT/GNP(6nM)-h upon successive H_2O_2 additions at a polarization potential of –0.80 V. The concentration of H_2O_2 was increased from 0 to 0.1 mM during the first five additions, and from 0.1 to 10 mM in the following eight additions. (d) Calibration plot obtained from graph (c).

Chronoamperometric experiments with different additions of H_2O_2 were performed for the Alg/PEDOT/GNP(6nM)-h using a polarization potential of –0.80 V, as observed in Figure 8c. A very small concentration of H_2O_2 was added in the first five additions, reaching concentrations of 0.01, 0.025, 0.05, 0.075 and 0.1 mM, while it was significant increased (from 0.1 to 10 mM) in the last eight additions. The analytical curve of the examined hydrogel, which is displayed in Figure 8d, indicates that the sensor works in

20

two regimes, one for concentrations ≤ 0.1 mM ($R^2 = 0.995$), and the other for concentrations ranging from > 0.1 mM to 10mM ($R^2 = 0.988$).

Thus, the sensor covers a good response mainly in the range normal (first regime) and moderately toxic – more toxic (second regime) to human body, respectively. This change in the slope is attributed to the fact that at low concentration of H_2O_2 (first regime) there is no excess of H_2O_2 and OH^- in the sensing medium to self-promote the reaction among them. Instead, in the second regime the excess of H_2O_2 and OH^- probably promotes the formation of oxygen reactive species (ROS). The LOD obtained for the first and second regimes are 0.02 µM and 10.6 µM, respectively.

L-lactate detection using LOx-functionalized Alg/PEDOT/GNP(6nM) sensor

Finally, a real enzymatic sensor was prototyped by immobilizing the lactate oxidase LOx enzyme on the Alg/PEDOT/GNP(6nM)-h. For this purpose, the procedure reported by Currano *et al.* [48] was adapted. More specifically, 30 µL of a mixture of LOx (100 U/mL), bovine serum albumin (25 mg/mL) and glutaraldehyde (2.5 wt.%), which delivered 15.4 U/mL of LOx per sample, were deposited on the hydrogel. Samples were allowed to dry for 24 h. The success of the immobilization process and the performance of the sensor were demonstrated using L-lactate solutions at varied concentrations, which ranged from 1 to 100 mM. The voltammetric response of the control (*i.e.* Alg/PEDOT/GNP(6nM) without LOx) and the LOx-functionalized sensor to the solutions with different L-lactate concentrations is shown in Figure 9a-b. The biosensors were maintained in contact with the corresponding L-lactate solution for 5 min before recording the CV.

The current density at –0.80 V (in absolute value) increased with increasing L-lactate concentrations for the LOx-functionalized biosensor (Figure 9b), while the current

density remained stable for the control (Figure 9a). Representation of the current density at such potential versus the concentration of L-lactate evidenced a linear behavior with $R^2 = 0.9354$ from 10 to 100 mM (Figure 9c). The calibration plot indicates that the sensitivity and the LOD in such high concentration interval was of 0.0216 $\mu A/(cm^2 \cdot mM)$ and 3.5 mM, respectively. In order to analyze the behavior at lower L-lactate concentrations, additional assays were performed using solutions with L-lactate concentrations ranging from 0.1 to 5 mM (Figure 9c and inset). At such low concentration values, the current density also exhibits a linear decreasing profile with increasing L-lactate concentration, even though with a different slope (*i.e.* an inflection point appears). This change in the slope is fully consistent with that displayed in Figure 8d and has been attributed to the low amount of H_2O_2 and OH^- in the sensing medium. Accordingly, the diffusion of H_2O_2 molecules capable of reaching the electrode is the only expected contribution in such conditions, whereas the plot for higher concentrations (after the inflection point) is probably affected by the formation of ROS. For the low concentrations tract, the LOD decreases to 0.4 mM.

All in all, the performance of LOx-functionalized Alg/PEDOT/GNP(6nM)-h is appropriate to detect L-lactate in a wide number of biological fluids (*e.g.* venous blood, sweat and capillary blood) in which the concentration of the bioanalyte is significantly higher either before or after exercise than the LOD of the developed biosensor [49]. For example, the concentration of L-lactate in venous blood, sweat and capillary blood before / after exercise was measured to be 3.0 ± 0.5 / 7.2 ± 0.7 mM, 20.4 ± 6.7 / 62.2 ± 16.3 mM and 1.6 ± 0.5 / 9.7 ± 1.2 mM, respectively [49].
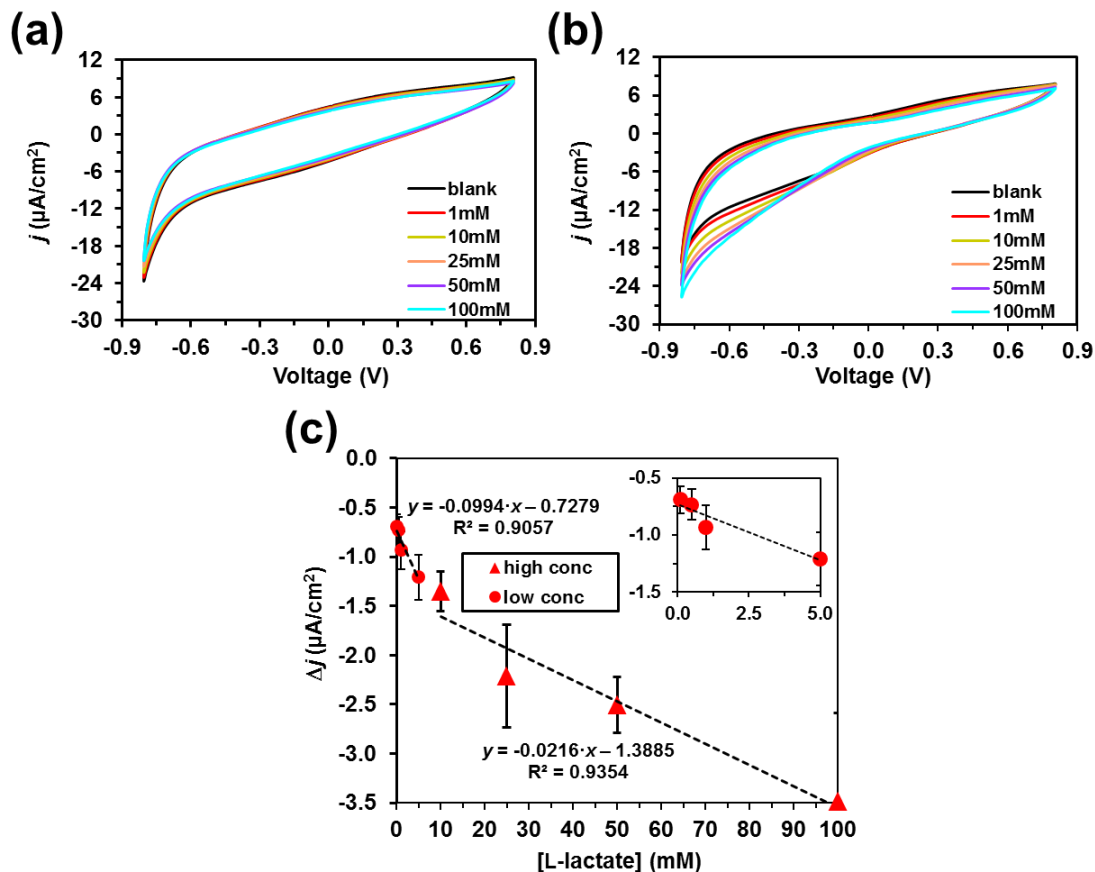
Figure 9. Cyclic voltammograms recorded from –0.8 to 0.8 V at a scan rate of 100 mV/s for (a) non-functionalized and (b) LOx-functionalized Alg/PEDOT/GNP(6nM)-h using solutions with different concentrations of L-lactate concentrations, from 0 (blank) to 100 mM. (c) Calibration plot obtained from graph (b).

Conclusions

A conductive hydrogel nanocomposite has been developed for the analysis of L-lactate. This consists on a hydrogel formed by an interpenetrated network of Alg and PEDOT, loaded with GNP. After characterization of the hydrogel composite, the conditions for the detection of H_2O_2 were optimized by considering different GNP concentrations. It has been found that 6 nM GNP amplifies the voltammetric and chronoamperometric signals associated to the electrochemical reduction of H_2O_2. The Alg/PEDOT/GNP(6nM)-h sensor was found to detect H_2O_2 concentrations covering the

range from normal to toxic. After that, the LOx enzyme was immobilized on the surface of the Alg/PEDOT/GNP(6nM)-h sensor using a simple, rapid, and reproducible procedure. The enzyme catalyzes the oxidation of L-lactate to pyruvate, allowing for a stable signal to be recorded following the oxidation of the enzymatically produced H_2O_2. Because of its excellent performance, the proposed LOx-functionalized sensor could be employed for the screening of L-lactate in a large number of biofluids, where typical concentrations lie in the range of 1.6 and 62 mM. In addition to its potential for clinical diagnosis, the sensor fulfills the conditions required for applications in other fields, like food analysis and biotechnology.

Conflicts of interest

There are no conflicts to declare.

Acknowledgements

References

[1] J. K: Wang, N. M. J. Cheam, S. A. Irvine, N. S. Tan, S. Venkatraman, C. Y. Tay, Interpenetrating network of alginate-human adipose extracellular matrix hydrogel for islet cells encapsulation. Macromol. Rapid. Commun. 41 (2020) 2000275.

[2] H. L. Yi, S. Forsythe, Y. Y. He, Q. Liu, G. Xiong, S. C. Wei, G. D. Li, A. Atala, A. Skardal, Y. Y. Zhang, Tissue-specific extracellular matrix promotes myogenic differentiation of human muscle progenitor cells on gelatin and heparin conjugated alginate hydrogels. Acta Biomater. 52 (2017) 222–233.

[3] D. Das, H. T. T. Pham, S. Lee, I. Noh, Fabrication of alginate-based stimuli-responsive, non-cytotoxic, terpolymeric semi-ipn hydrogel as a carrier for controlled release of bovine albumin serum and 5-amino salicylic acid. Mat. Sci. Eng. C Mater. 98 (2019) 42–53.

[4] S. Kim, S. Jung, Biocompatible and self-recoverable succinoglycan dialdehyde-crosslinked alginate hydrogels for ph-controlled drug delivery. Carbohydr. Polym., 250 (2020) 116934.

[5] M. Liu, X. Song, Y. T. Wen, J. L. Zhu, Injectable thermoresponsive hydrogel formed by alginate-*g*-poly(n-isopropylacrylamide) that releases doxorubicin-encapsulated micelles as a smart drug delivery system. ACS Appl. Mater. Interfaces, 9 (2017) 35673–35682.

[6] A. Puiggalí-Jou, E. Cazorla, G. Ruano, I. Babeli, M.-P. Ginebra, J. García-Torres, C. Alemán, Electroresponsive alginate-based hydrogels for controlled release of hydrophobic drugs. ACS Biomater. Sci. Eng. 6 (2020) 6228–6240.

[7] C. T. Moody, S. Palvai, Y Brudno, Click cross-linking improves retention and targeting of refillable alginate depots. Acta Biomater. 112 (2020) 112–121.

[8] M. M. Pérez-Madrigal, J. E. Shaw, M. C. Arno, J. A. Hovland, S. M. Richardson, A. P. Dove, Robust alginate/hyaluronic acid thiol-yne click-hydrogel scaffolds with superior mechanical performance and stability for load-bearing soft tissue engineering. Biomater. Sci. 8 (2020) 405–412.

[9] C. H. Jang, Y. W. Koo, G. H. Kim, ASC/chondrocyte-laden alginate hydrogel/pcl hybrid scaffold fabricated using 3d printing for auricle regeneration. Carbonhydr. Polym. 248 (2020) 116776.

[10] H. F. Yuan, X. Y. Zheng, W. Liu, H. Zhang, J. Shao, J. X. Yao, C. Y. Mao, J. F. Hui, D. D. Fan, A Novel bovine serum albumin and sodium alginate hydrogel scaffold doped with hydroxyapatite nanowires for cartilage defects repair. Colloids Surf. B 192 (2020) 111041.

[11] S. Pina, J. M. Oliveira, R. L. Reis, Natural-based nanocomposites for bone tissue engineering and regenerative medicine: A review. Adv. Mater. 27 (2015) 1143–1169.

[12] M. M. Pérez-Madrigal, J. Torras, J. Casanovas, M. Haring, C. Alemán, D. D. Diaz, Paradigm shift for preparing versatile m^{2+}-free gels from unmodified sodium alginate. Biomacromolecules 18 (2017) 2967–2979.

[13] G. T. Grant, E. R. Morris, D. A. Rees, P. J. Smith, D. Thom, biological interactions between polysaccharides and divalent cations: The egg-box model. FEBS Letters, 32 (1973) 195–198.

[14] A. Serafin, C. Murphy, M. C. Rubio, M. N. Collins, printable alginate/gelatin hydrogel reinforced with carbon nanofibers as electrically conductive scaffolds for tissue engineering. Mater Sci. Eng. C 122 (2021) 111927.

[15] L. Mottet, D. Le Cornec, J. M. Noel, F. Kanoufi, B. Delord, P. Poulin, J. Bibette, N. A. Bremond, A conductive hydrogel based on alginate and carbon nanotubes for probing microbial electroactivity. Soft Matter 14 (2018) 1434–1441.

[16] T. Distler, C. Polley, S. Fukun, D. Schneidereit, M. D. Ashton, O. Friedrich, J. F. Kolb, J. G. Hardy, R. Detsch, H. Seitz, A. R. Boccaccini, Electrically conductive

and 3d-printable oxidized alginate-gelatin polypyrrole:pss hydrogels for tissue engineering. Adv. Healthcr. Mater. 10 (2021) 2001876.

[17] Y. Q. Li, X. H. Liu, Q. Gong, Z. B. Xia, Y. Yang, C. Chen, C. H. Qian, Facile preparation of stretchable and self-healable conductive hydrogels based on sodium alginate/polypyrrole nanofibers for use in flexible supercapacitor and strain sensors. Int. J. Biol. Macromol. 172 (2021) 41–54.

[18] I. Babeli, G. Ruano, J. Casanovas, M. P. Ginebra, J. García-Torres, C. Alemán, Conductive, self-healable and reusable poly(3,4-ethylenedioxythiophene)-based hydrogels for highly sensitive pressure arrays. J. Mater. Chem. A 8 (2020) 8654–8667

[19] K. Ren, Y. Cheng, C. Huang, R. Chen, Z. Wang, J. Wei, Self-healing conductive hydrogels based on alginate, gelatin and polypyrrole serve as a repairable circuit and a mechanical sensor. J. Mater. Chem. B 7 (2019) 5704–5712.

[20] S. Yang, L. K. Jang, S. Kim, J. Yang, K. Yang, S. W. Cho, J. Y. Lee, Polypyrrole/alginate hybrid hydrogels: electrically conductive and soft biomaterials for human mesenchymal stem cell culture and potential neural tissue engineering applications. Macromol. Biosci. 16 (2016) 1653–1661.

[21] F. Zhong, M. Ma, Z. Zhong, X. Lin, M. Chen, Interfacial growth of free-standing pani films: toward high-performance all-polymer supercapacitors. Chem. Sci. 12 (2021) 1783–1790.

[22] F. Liesa, C. Ocampo, E. Armelin, R. Oliver, F. Estrany, C. Alemán, Application of electrochemically produced and oxidized poly (3,4-ethylenedioxythiophene) as anticorrosive additive for paints: influence of the doping level. J. Appl. Polym. Sci. 12 (2006) 1592–1599.

[23] L. P. Zhang, B. Wang, X. B. Li, G. P. Xu, S. L. Dou, X. Zhang, X. Chen, J. P. Zhao, K. Zhang, Y. Li, Further understanding of the mechanisms of electrochromic devices with variable infrared emissivity based on polyaniline conducting polymers. J. Mater. Chem. C 7 (2019) 9878–9891.

[24] J. G. Wu, J. H. Chen, K. T. Liu, S. C. Luo, Engineering antifouling conducting polymers for modern biomedical applications. ACS Appl. Mater. Interfaces 11 (2019) 21294–21307.

[25] Kenry, B. Liu, Recent advances in biodegradable conducting polymers and their biomedical applications. Biomacromolecules 19 (2018) 1783–1803.

[26] X. X. Fu, W. Q. Zeng, A. C. Ramirez-Perez, G. Lisak, 3-D and electrically conducting functional skin mapping for biomedical applications. Chem. Commun. 54 (2018) 980–983.

[27] G. X. Wang, A. Morrin, M. R. Li, N. Z. Liu, X. L. Luo, Nanomaterial-doped conducting polymers for electrochemical sensors and biosensors. J. Mater. Chem. B 6 (2018) 4176–4190.

[28] M. Martí, G. Fabregat, F. Estrany, C. Alemán, E. Armelin, Nanostructured conducting polymer for dopamine detection. J. Mater. Chem. 20 (2010) 10652–10660.

[29] R. K. Pal, S. C. Kundu, V. K. Yadavalli, Fully organic, degradable energy storage devices using silk proteins. ACS Appl. Mater. Interfaces 10 (2018) 9620−9628.

[30] G. Fabregat, B. Teixeira-Dias, L. J. del Valle, E. Armelin, F. Estrany, C. Alemán, Incorporation of a clot-binding peptide into polythiophene: properties of composites for biomedical applications. ACS Appl. Mater. Interfaces 6 (2014) 11940–11954.

[31] M. J. Donahue, A. Sanchez-Sanchez, S. J. Qu, R. M. Owens, PEDOT properties for applications in bioelectronics. Mater. Sci. Eng. R Reports 140 (2020) 100546.

[32] T. J. Zajdel, M. Baruch, G. Méhes, E. Stavrinidou, M. Berggren, M. M. Maharbiz, D. T. Simon, C. M. Ajo-Franklin, PEDOT:PSS-based multilayer bacterial-composite films for bioelectronics. Sci. Rep. 8 (2018) 15293.

[33] P. Pananon, C. Sriprachuabwong, A. Wisitsoraat, P. Chuysinuan, A. Tuantranont, P. Saparpakorn, D. Dechtrirat, A facile one-pot green synthesis of gold nanoparticle-graphene-pedot:pss nanocomposite for selective electrochemical detection of dopamine. RSC Adv. 8 (2018) 12724–12732.

[34] J. Turkevich, P. C. Stevenson, J. A. Hillier, A study of the nucleation and growth processes in the synthesis of colloidal gold. Discuss. Faraday Soc. 11 (1951) 55–75.

[35] P. Zhao, N. Li, D. Astruc, State of the art in gold nanoparticle synthesis. Coord. Chem. Rev. 257 (2013) 638–665.

[36] W. C. Oliver, G. M. Pharr, An improve technique for determining hardness and elastic modulus using load and displacement sensing indentation experiments. J. Mater. Res. 7 (1992) 1564–1583.

[37] W. C. Oliver, G. M. Pharr, Measurement of hardness and elastic modulus by instrumented indentation: advances in understanding and refinements to methodology. J. Mater. Res. 19 (2004) 3–20.

[38] C. R. Mayer, S. Neveu, V. Cabuil, Hybrid nanonetworks from gold-functionalized nanoparticles. Adv. Mater. 14 (2002) 595–597.

[39] S. W. Han, Y. Kim, K. Kim, Dodecanethiol-derivatized au/ag bimetallic nanoparticles: tem, uv/vis, xps, and ftir analysis. J. Colloid Interface Sci. 208 (1998) 272–278.

[40] M. M. Campos-Vallette, N. P. Chandía, E. Clavijo, D. Leal, B. Matsuhiro, I. O. Osorio-Román, S. Torres, Characterization of sodium alginate and its block fractions by surface-enhanced raman spectroscopy. J. Raman Spectrosc. 41 (2010) 758–763.

[41] R. V. Salvaterra, L. G. Moura, M. M. Oliveira, M. A. Pimienta, A. J. G. Zarbin, Resonant Raman spectroscopy and spectroelectrochemistry characterization of carbon nanotubes/polyaniline thin film obtained through interfacial polymerization. J. Raman Spectrosc. 43 (2021) 1094–1100.

[42] M. Cavo, M. Fato, L. Peñuela, F. Beltrame, R. Raiteri, S. Scaglione, Microenvironment complexity and matrix stiffness regulate breast cancer cell activity in a 3D in vitro model. Sci. Rep. 6 (2016) 35367.

[43] B. G. Molina, S. Cuesta, H. Besharatloo, J. J. Roa, E. Armelin, C. Alemán, Free-standing faradaic motors based on biocompatible nanoperforated poly(lactic acid) layers and electropolymerized poly(3,4-ethylenedioxythiophene). .ACS Appl. Mater. Interfaces 11 (2019) 29427–29435.

[44] K. Rathee, V. Dhull, R. Dhull, S. Singh, Biosensors based on electrochemical lactate detection: A comprehensive review. Biochem. Biophys. Rep. 5 (2016) 35–54.

[45] F. Alam, S. Roy Choudhury, A. H. Jalal, Y. Umasankar, S. Forouzanfar, N Akter, S. Bhansali, N. Pala, Lactate biosensing: The emerging point-of-care and personal health monitoring. Biosens. Bioelectron. 15 (2018) 818–829.

[46] L. Rassaei, W. Olthuis, S. Tsujimura, E. J. R. Sudhölter, A. van den Berg, Lactate biosensors: Current status and outlook. Anal. Bioanal. Chem. 406 (2014) 123–137.

[47] A. Forootan, R. Sjöback, J. Björkman, B. Sjögreen, L. Linz, M. Kubista, Methods to determine limit of detection and limit of quantification in quantitative real-time PCR (qPCR). Biomol. Detect. Quantif. 12 (2017) 1−6.

[48] L. J. Currano, F. C. Sage, M. Hagedon, L. Hamilton, J. Patrone, K. Gerasopoulos, Wearable sensor system for detection of lactate in sweat. Sci. Rep. 8 (2018) 15890.

[49] D. A. Sakharov, M. U. Shkurnikov, M. Yu Vagin, E. I. Yashina, A. A. Karyakin, A. G. Tonevitsky, Relationship between lactate concentrations in active muscle sweat and whole blood. B. Exp Biol. Med. 150 (2010) 83−85.

Graphical abstract